Ab Initio Molecular Dynamics Study of 45S5 Bioactive Silicate Glass

Antonio Tilocca*,† and Nora H. de Leeuw†,‡

Department of Chemistry, University College London, London, United Kingdom, and School of Crystallography, Birkbeck College, London, United Kingdom

Bioglass 45S5, the prototype of bioactive melt-quenched silicate glasses, was modeled by means of Car−Parrinello molecular dynamics (CPMD) simulations. Although long-range structural properties cannot be modeled by using this ab initio approach, the accuracy of CPMD simulations is exploited here to provide insight into the short-range structure and to analyze vibrational and electronic properties of this biomaterial. Detailed structural analysis in the short-range scale provided insight into the local environment of modifier Na and Ca ions: a possible key role of these cations in organizing the glass network by connecting different chains and fragments into specific, rather flexible geometries was proposed. The individual contributions of different species to the vibrational density of states were separated and discussed, allowing the identification of specific features in the vibrational spectrum, such as those related to phosphate groups. The components of the electronic density of states were also analyzed, enabling us to identify correlations between the electronic structure and the structural properties, such as the different bonding character of Si−O bonds involving bridging or nonbridging oxygen atoms.

1. Introduction

Some compositions of melt-quenched phosphosilicate glasses are classified as bioactive because of the strong chemical response they elicit upon contact with a physiological medium, involving partial dissolution, followed by nucleation of an amorphous calcium phosphate layer, which eventually crystallizes into a hydroxy-carbonate apatite (HCA) layer.[1,2] When the glass is implanted in the human body, the formation of a crystalline HCA layer has a crucial role in providing a strong, stable interfacial link between the implanted material and the living tissues, making these materials suitable for restorative and regenerative biomedical applications such as orthopaedic, otolaryngological, dental, and maxillofacial implants.[3,4] Since the rate at which the HCA crystallization occurs is crucial for the success of biomedical applications, the bioactivity of these materials is often measured in terms of the rate of HCA formation.[5-7] This rate is strongly affected by the composition: the 45S5 Bioglass composition, containing 45% of silica, crystallizes HCA on its surface very rapidly, and can bind to both soft and hard tissues; the bioactivity sharply decreases with increasing silica content, and no HCA crystallization is observed for similar melt-quenched compositions with more than 60% SiO_2.[1] Among other experimental methods, Raman and infrared vibrational spectroscopy techniques are frequently employed to probe the structural features of different compositions[8,9] and to highlight the structural changes which characterize the bioactive response.[6,7,10] A common problem with investigations of these materials, generally related to their amorphous nature, is the lack of detailed information on the microscopic structure of the glasses and how this structure is affected by the composition. The atomistic resolution provided by computer simulations, benefitting from the availability of increasingly more powerful high-performance computers and from continuous advances in

theoretical methods,[11] can be extremely useful in complementing and supporting experiments toward a more fundamental understanding of the properties of these materials. Classical molecular dynamics (MD) simulations are well suited to model simple silicate and phosphate glasses;[12-17] however, multicomponent phosphosilicate glasses may represent a challenge for classical MD, due to the difficulty of incorporating many different interactions and complex effects in a reliable force field. An alternative computational approach, unhindered by the need to develop an accurate potential model due to its first-principle calculation of energy and ionic forces, is represented by ab initio molecular dynamics (AIMD), such as the Car−Parrinello method.[18,19] This approach has been successfully applied to investigate structural and electronic effects in silica and modified silicate glasses.[20-24] The large computational resources needed by the explicit inclusion of electronic degrees of freedom limit the properties which can be effectively explored in AIMD simulations of glasses: structural features beyond local order, such as network connectivity or the Q^n distribution, as well as long-range ionic migration pathways, lie outside the space/time ranges accessible with AIMD. On the other hand, the ionic vibrational motion in condensed phases can be adequately sampled in AIMD simulations, and they have been successfully employed to determine vibrational and elastic properties of silicate glasses.[22,25,26] In addition, AIMD simulations give straightforward access to the electronic properties of glasses,[27,28] which are essential to complete the picture of the bulk properties of these materials related to their bioactivity.

In this paper, we report on Car−Parrinello molecular dynamics (CPMD) simulations of the 45S5 Bioglass; this is a highly bioactive composition, commonly used in biomedical applications, and probably the most studied composition among the Hench's silicate bioglasses. The outline of this work is as follows: first, we discuss basic structural properties as obtained from the simulations, showing the reliability of the present computational approach to model bioactive silicate glasses and

---
* Address correspondence to this author. E-mail: a.tilocca@ucl.ac.uk.
† University College London.
‡ Birkbeck College London.

TABLE 1: Details of the Simulated Glass

	SiO_2	Na_2O	CaO	P_2O_5	cell side, Å
mol %	46.3	24.39	26.82	2.44	11.63
N of species	19	10	11	1	

providing new insight; then, we determine and discuss vibrational and electronic properties of these materials, highlighting the contributions of the different species to the vibrational and electronic density of states of this glass.

2. Computational Methods

The 45S5 composition contains 45% SiO_2 in weight, a low amount (6 wt %) of P_2O_5, and an equal percentage (24.5 wt %) of Na_2O and CaO. Previous studies showed that a periodically repeated cell of 10 Å sides reproduces the local structure and dynamics of silicate glasses accurately.[21,24,28] With a slightly larger cubic cell side (11.63 Å), the composition used in this work, reported in Table 1, corresponds to the glass density at room temperature[29] of 2.66 g cm^{-3}.

In MD simulations of melt-quenched glasses, the molten glass is quenched to room temperature at typical cooling rates around 10 deg/ps. The CPU time required for a full CPMD quench to room temperature at such cooling rates (which are already much faster than in experimental procedures) would be prohibitively long. Therefore, following a standard approach for ab initio MD,[22,24,28] the quenching procedure is carried out by using classical MD, before switching to CPMD once the initial glass structure has been obtained. In the classical MD quench we employed the DLPOLY code[30] with a shell-model potential recently developed in our group, which allows the modeling of modified silicate glasses with the inclusion of polarization effects.[31] This potential, incorporating Buckingham pair potentials and three-body angular terms besides the core−shell description of oxide ions, has been succesfully applied to simulate silicate glasses[31] and was recently extended to include the interaction with phosphate groups.[32] A 0.2 fs time step was used in the classical MD runs, small enough to control the high frequency of the core−shell spring, and a cutoff distance of 8 Å was applied to the van der Waals interactions. A random initial configuration was heated for 60 ps at 5000 K, and then continuously cooled to 300 K in 470 ps, with a 10 deg/ps linear cooling rate. The quenched structure was then used to start a final 200 ps NVT run at room temperature, ensuring adequate thermalization of our relatively small glass samples. The final configuration was then used as a starting point for the CPMD simulation. CPMD runs at constant volume were carried out with use of the CP code included in the Quantum-ESPRESSO package,[33] whereas the PWSCF code of the same package was used for structural optimizations and electronic structure calculations. The electronic structure was described by the Generalized Gradient Approximation (GGA) to density functional theory (DFT), using the PBE exchange-correlation functional.[34] Vanderbilt ultrasoft pseudopotentials[35] represented core−valence electron interactions for all atomic species; semicore shells were explicitly included for Na and Ca. Plane-wave basis set cutoffs for the smooth part of the wavefunctions and the augmented density were set to 30 and 200 Ry and k-sampling was restricted to the Γ point in the calculations. The time step and fictitious electronic mass μ were set to 0.145 fs and 700 au, respectively. This computational setup was extensively tested, and it has recently been used to model modified silicate glasses with good accuracy.[21,31] Moreover, previous ab initio simulations (with methods and supercell sizes close to the ones employed in the present work)[20,22,28] have proven the

TABLE 2: Coordination Statistics from the CPMD Simulations

Q^n Distribution (%)						
	Q^0	Q^1	Q^2	Q^3	Q^4	Q^5
Si	5.3	18.4	52.6	13.2	10.5	0
P	50	50	0	0	0	0

Coordination (%)					
NBO	BO	O_3c	Si_4c	Si_5c	P_4c
68.8	31.2	0	100	0	100

Oxygen Coordination Number			
	O	NBO	BO
Si	4.0	1.95	2.05
P	4.0	3.5	0.5
Na	5.75	4.5	1.25
Ca	6.0	5.4	0.6

accuracy of the current approximations in determining structural, dynamical, and electronic properties of glasses. To enlarge the portion of the configuration space probed by our MD simulations and improve their statistical accuracy, two glass samples were modeled, obtained by starting the melt-and-quench procedure from different random configurations. A CPMD trajectory of ∼10 ps in the NVT ensemble at room temperature was carried out for each sample, where the first 4 ps were not included in the structural and dynamics analysis. Structural and dynamical results were further averaged over the two samples. The velocity time autocorrelation function (VACF) was calculated from the MD trajectory, and Fourier transformed to provide the vibrational density of states (VDOS) for each glass. The use of a fictitious electronic mass in CPMD leads to an artificial drag on the nuclear motion, which may affect properties explicitly dependent on the ionic masses, such as the power spectrum;[36,37] the calculated VDOS was then corrected by evaluating the VDOS from an additional MD trajectory with $\mu = 300$ au, and extrapolating to zero fictitious electronic mass.[38] Partial VACFs were also calculated, allowing us to project out the contribution of each atomic species to the vibrational spectrum. Total and projected electronic density of states (EDOS) were calculated on locally optimized structures, including a number of empty states equal to 20% of the number of occupied states.

3. Results and Discussion

3.1. Initial Structure. The medium-range structural features such as Q^n distribution (where Q^n denotes a Si or P ion bonded to n bridging oxygens) and network connectivity are determined by the glass generation with classical MD and can hardly be modified after switching to the ab initio dynamics, due to the short time scale of the latter.[28] Indeed, the Q^n and coordination statistics calculated from the CPMD runs (Table 2) are unchanged with respect to the initial glass structure obtained from classical MD; since this initial medium-range structure is maintained in CPMD, it is important to ensure that it is qualitatively accurate. Among other properties, the microscopic structural features of a glass generated by computer simulations are significantly affected by the cooling rate; however, most structural properties—including properties beyond the short range, such as ring size distributions—appear sufficiently converged for rates close to 10 deg/ps,[39] which is therefore the commonly adopted value for the cooling rate in MD simulations of melt-derived glasses.[15−17,40] Residual inaccuracies in glass structures quenched at this rate are more likely to be related to other issues, such as the small size of the (infinitely periodic) supercell. From this perspective, it is important that the Q^n
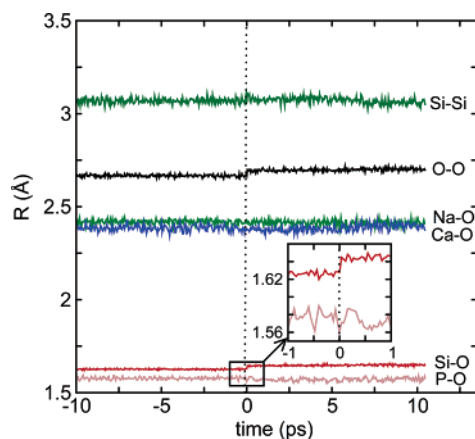
Figure 1. Time evolution of several average distances in the last 10 ps of the classical MD run and in the subsequent CPMD trajectory, which starts at $t = 0$. The inset shows an enlargement of the Si−O and P−O average distances close to $t = 0$.
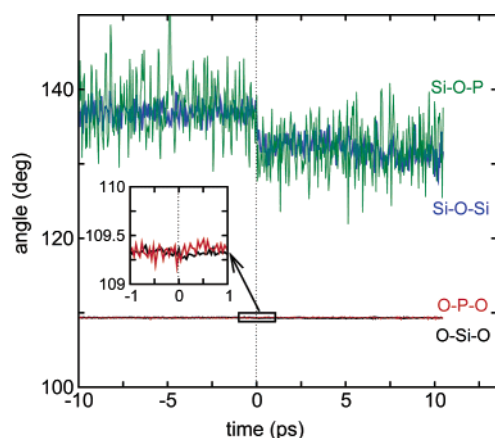

Figure 2. Time evolution of O−T−O and T−O−T average angles in the last 10 ps of the classical MD run and in the subsequent CPMD trajectory, which starts at $t = 0$. The inset shows an enlargement of the O−Si−O and O−P−O average angles close to $t = 0$.

distribution reported in Table 2, showing a net predominance of Q^2(Si) species, is in qualitative agreement with Raman spectroscopy data,[41] which also yield a distribution centered at $n = 2$.

Although the cooling procedure and the following simulations are carried out in the NVT ensemble, at the fixed volume corresponding to the experimental glass density, it is worth estimating the theoretical density of the glass obtained by classical MD, since the density can be affected by the cooling rate.[39] The average pressure (~6 kbar) in the final NVT run with classical MD is reasonable for these kind of systems and empirical potentials,[42] and it leads to a theoretical density (averaged over an NPT run of 20 ps at standard temperature and pressure) 1.2% smaller than the experimental one.

3.2. Local Order. At variance with the medium-range structure, relevant properties reflecting the short-range order, such as local coordination environments and bond distances and angles around tetrahedral Si and P sites (as well as vibrational properties) can fully relax to the ab initio values. The time evolution of several average distances in the last 10 ps of the classical MD run and in the following CPMD trajectory is shown in Figure 1, whereas the corresponding trajectories of average O−T−O and T−O−T angles are shown in Figure 2. After switching to CPMD, there is a small increase (around 1.5%) in the average distances of both Si−O and O−O,[43] whereas no changes in Si−Si distance are observed. A small increase in

the average Ca−O distance leads it to overlap with the Na−O distance, which is unaffected by the switch to CPMD. The intratetrahedral geometry, as represented by the O−T−O angles in Figure 2, is essentially unchanged, which is expected since the three-body terms in the potential model constrain these angles to their correct values in the classical MD run. Despite the larger fluctuations in the average T−O−T angles, due to the smaller number of these links (especially Si−O−P) in the simulation cell, it is possible to measure a ~5° decrease of both Si−O−Si and Si−O−P angles, correlated to the longer Si−O distance. These rearrangements of the local glass structure are completed shortly after "turning on" the Car−Parrinello dynamics; to further confirm that structural relaxation is completed in the time spanned by the CPMD trajectories, we compared coordination statistics, radial distribution functions (rdfs), and bond angle distributions (BADs) calculated by using either the first or the second half of the CPMD trajectory: no significant differences are apparent, besides those due to the less accurate statistics resulting from the inclusion of only half of the trajectory data in the analysis (see the Supporting Information).

Compared to a fully interconnected silicate network such as vitreous silica (VS), the inclusion of modifier Na and Ca oxides leads to the breaking of Si−BO−Si bonds (where BO is a bridging oxygen) and their replacement by Si−NBO···M links (where NBO is a nonbridging oxygen, and M is a Na or Ca cation).[44] The Q^n distribution is then shifted from 100% Q^4 for VS to lower n values, with a prevalence of Q^2 and Q^3 species, for 45S and similar compositions.[41,45] The coordination statistics from the CPMD runs, summarized in Table 2, denote ideal tetrahedral coordination for both silicon and phosphorus, with no under- or over-coordinated defects, such as 3-fold coordinated oxygens (O_{3c} in the table) and 5-fold coordinated silicon (Si_{5c}). The overall NBO:BO ratio reflects a 2:2 ratio in the SiO_4 tetrahedra, and a much higher NBO fraction in PO_4 groups; indeed, the calculated Q^n distribution for Si denotes the prevalence of metasilicate Q^2 species, forming chain-like silicate fragments, whereas phosphate is found either isolated (Q^0) or as pyrophosphate Q^1 where only one of its four oxygens forms a bridge with an adjacent silicon. The local structure of the glass is summarized in the radial and angular distribution functions plotted in Figures 3 and 4. The total radial distribution functions relative to the O atoms, plotted in the bottom panel of Figure 3, are projected onto the NBO/BO components in the upper panels. The P−O bond length of 1.55 Å (estimated as the peak position in the corresponding rdf) is shorter than the Si−O one (1.63 Å); in general, T−NBO bonds (T = Si, P) are stronger than T−BO, and the dominance of NBOs in the P coordination shell accounts for this difference. Moreover, Figure 3b shows that P−NBO bonds are significantly shorter than Si−NBO bonds, and P−BO bonds are also slightly shorter than Si−BO. In ref 46 a mean P−O distance of 1.55 Å was obtained by neutron diffraction for several phosphate glass compositions, containing P−NBO bonds generally around 0.1−0.15 Å shorter than P−BO. The decomposition of T−O peaks into the BO/NBO components in Figure 3b thus shows that the different strength of P−BO and P−NBO bonds is well reproduced by our simulations, and similar considerations apply to Si−O bonds: in this case we can compare our calculated r(Si−BO)−r(Si−NBO) of 0.06 Å with the 0.07 Å difference predicted by CPMD−GGA calculations of sodium silicate glasses.[28] The intratetrahedral BO−BO distance of 2.66 Å increases to 2.69 Å and to 2.71 Å for NBO−BO and NBO−NBO pairs (Figure 3b), denoting higher repulsion between NBO ions, which is related to their higher negative charge, as will be discussed
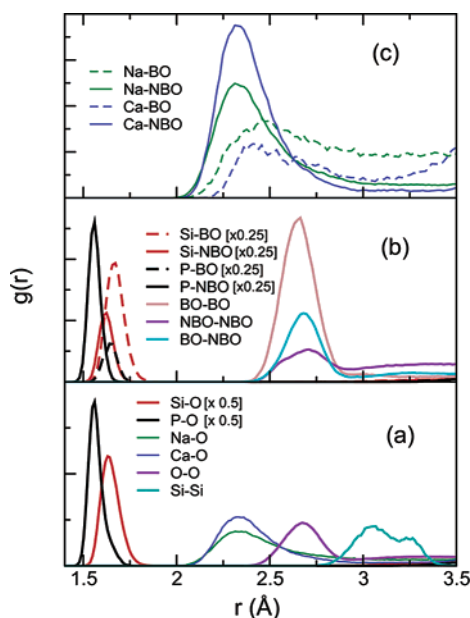
Study of 45S5 Bioactive Silicate Glass

J. Phys. Chem. B, Vol. 110, No. 51, 2006 **25813**

Figure 3. (a) Radial distribution functions averaged over the two 45S5 bioglass samples; (b) decomposition of the Si−O and P−O peaks into their NBO and BO components; and (c) decomposition of the Na−O and Ca−O peaks into their NBO and BO components.
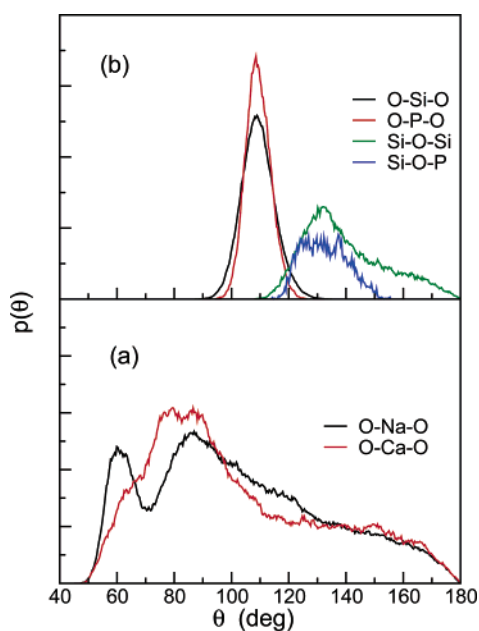

Figure 4. Angle distribution functions: (a) O−Na−O and O−Ca−O angles and (b) O−Si−O, O−P−O, Si−O−Si, and Si−O−P angles.

below. The different height of the above O−O peaks reflects the local, intratetrahedral scale examined in Figure 3: the short-range environment of a BO contains a larger number of oxygens, compared to an NBO, since NBO−NBO pairs often exhibit longer distances, beyond the intratetrahedral scale plotted in the figure. In other words, distances involving BOs tend to be concentrated on the local scale, whereas distances involving NBOs cover a wider range, and the height of the corresponding short-distance peak is lower.

The Na−O and Ca−O peak positions are both 2.33 Å, in the range of X-ray and neutron diffraction measurements for phosphate and soda-lime silicate glasses[47,48] and of previous CPMD calculations.[21,28] The coordination shell of both Na and Ca is composed of ca. six O atoms (Table 2), whose arrangement is unveiled in the distribution of O−M−O angles in Figure 4a.
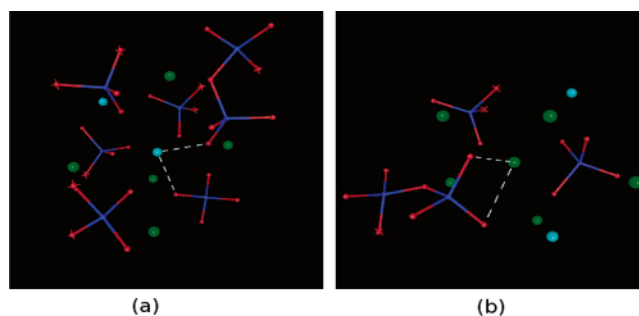

Figure 5. (a) Geometry of an intertetrahedral NBO−Ca−NBO link and (b) geometry of an intratetrahedral NBO−Na−NBO link. Silicon and oxygen atoms are shown as ball-and-stick, whereas Na and Ca are represented as spheres. Color codes are red (oxygen), blue (silicon), green (sodium), and cyan (calcium). The dashed lines highlight the relevant link. Crosses on some oxygen atoms represent points where the fragment shown in the picture has been cut out of the bulk structure.

Both distributions show a peak close to 90°, which generally results from Na or Ca atoms connecting two NBOs belonging to *different* tetrahedra, as shown in Figure 5a. This suggest an important structural role of modifier cations in controlling the folding of the silicate network by connecting and arranging together different chain-like and isolated fragments. The O−Na−O distribution also shows a sharp peak at 60°, which results from Na coordinated to two NBOs (or one NBO and one BO) belonging to the *same* tetrahedron, as in Figure 5b. This arrangement is less common for Ca, and only a shoulder at 60° is observed for the O−Ca−O angle distribution. The broad distributions of Figure 4a also denote a high flexibility of the geometries of the coordination shell of Na and Ca cations, with a wide range of angles allowed. Although the geometry of sodium and calcium coordination shells is qualitatively similar, the composition of these shells differs: there is a much higher fraction of NBOs in the Ca coordination shells, as can be inferred already by the relative areas of the M−BO and M−NBO peaks in Figure 3c and is quantitatively shown in Table 2. This marked preference of calcium for coordination by NBOs seems to be a common feature of other modified silicate glasses, and arises from the higher negative charge on NBOs, discussed in section 3.4.[21,31]

The intertetrahedral Si−O−Si angle (Figure 4b) of 132° is 5° smaller with respect to the Si−O−Si angle obtained with the same computational approach for a common soda-lime glass composition with a higher silica content;[21] this is due to the need to accommodate a larger number of modifier cations around the central (bridging) oxygen for Si−O−Si triads in 45S5. Although the poor statistics of the Si−O−P BAD in Figure 4, due to the low number of such links observed in our simulations, do not allow us to obtain a very accurate value for this angle, these links seem to have a similar, slightly more rigid, geometry to Si−O−Si.

3.3. Vibrational Properties. The total vibrational density of states (VDOS) is shown as a dashed line in Figure 6a. The high-frequency band exhibits a shoulder at 1100 cm^{-1} and two peaks at 1010 and 905 cm^{-1}; based on the VDOS projections in the same figure, the first feature is mainly related to phosphate and the other two are related to silicate groups. The high-frequency vibrational spectra of alkali and alkaline-earth silicate glasses are a combination of four bands, corresponding to ortho-, pyro-, meta-, and di-silicate species, at 850, 900, 950−1000, and 1050−1100 cm^{-1}, respectively.[49] Due to the highly localized character of vibrational modes in silicate glasses,[50] these features are likely to be transferable to different systems with similar silicate content and network structure. For bioactive composi-
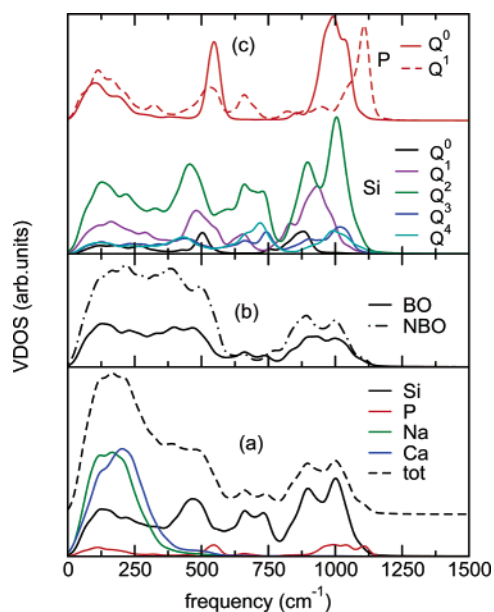
Figure 6. Vibrational density of states (VDOS) calculated and Fourier transform of the velocity autocorrelation function: (a) total and projected onto each atomic species; (b) projection onto BO and NBO atoms; and (c) projection onto each different $Si(Q^n)$ and $P(Q^n)$ site.
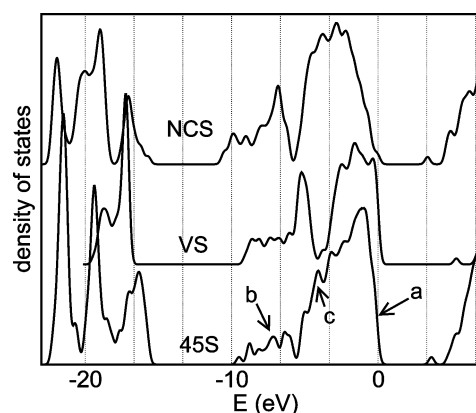

Figure 7. Electronic density of states (EDOS) for 45S bioactive glass (bottom panel: the arrows mark the energy of the states plotted in Figure 9a−c). The EDOS of VS and NCS glasses calculated in ref 21 are also shown for comparison. The curves are broadened with a Gaussian function of $\sigma = 0.25$ eV width and the highest occupied states are aligned at 0 eV.

tions, where metasilicates Q^2 dominate, absorption around 900−950 cm^{-1} is usually associated with Si−NBO−M (M = Na or Ca) vibrations, whereas absorption between 950 and 1100 cm^{-1} is assigned to asymmetric Si−BO stretching.[1,6,51−54] Our simulated spectra are in good agreement with these observations: a broad band between 800 and 1100 cm^{-1} characterizes the total VDOS in Figure 6a, with two main peaks at 905 and 1010 cm^{-1}. Looking at the projections of the vibrational spectrum onto the different Q^n (Si) sites in Figure 6c, it is clear that the two high-frequency peaks correspond to the dominant Q^2 species. Q^4 silicate species, with no NBOs in their coordination shell, show a single peak at 1010 cm^{-1}, whereas orthosilicate Q^0, surrounded by NBOs only, shows a single peak at 890 cm^{-1}. The high-frequency band of Q^1, Q^2, and Q^3 exhibits the transition between these two limits, with Q^2 representing the intermediate case where two NBOs and two BOs give rise to a double peak. While the total vibrational spectrum in Figure 6a tends to reflect the dominance of Q^2 silicates, the low fraction of phosphate results in a very weak shoulder at 1100 cm^{-1}, which arises from the Q^1 phosphate groups linked to a single Si (Figure 6c). It is interesting to observe that the formation of a single P−O−Si link (out of the four bonded oxygens) leads to a considerable blue-shift of the corresponding phosphate peak, with respect to the 1000 cm^{-1} frequency of the orthophosphate.

The region between 500 and 800 cm^{-1} is generally associated with Si−BO−Si vibrations in silicate glasses;[49] in particular, for bioactive compositions, bands in this region were assigned to ring[51,54] or rocking[53] vibrations and sometimes also to bending motion.[1,53] Indeed, the lack of vibrational intensity in the VDOS projected onto the orthosilicate species confirms the involvement of bridging oxygens in these vibrations. On the other hand, the same projection onto orthosilicate shows that the band at 480 cm^{-1}, which is sometimes assigned to Si−O−Si bending,[6,54] does not necessarily directly involve BOs. Another interpretation could be that the character of the vibration changes with the different connectivity of Q^n silicate units:[49] the peak is increasingly shifted toward lower frequencies as the percentage of bridging oxygens in the silicate increases.

The bottom part of the spectrum is dominated by the low-frequency (150−200 cm^{-1}) oscillations of Na and Ca ions around their NBO sites, with Ca vibrating at a slightly higher frequency.

An important issue in bioglass science involves the partial incorporation of phosphate units into the silicate network,[41,55,56] which may affect the phosphate release rate. Our classical MD-generated structures support this incorporation, and the AIMD simulations confirm that these links are rather stable. The low percentage of phosphate in these glasses might hinder the detection of Si−O−P features in IR and Raman spectra, whereas the projection onto phosphate of the simulated VDOS in Figure 6c allows us to identify possible markers of P−O−Si linkages: for instance, the 670 cm^{-1} peak, which is present in the Si−O−P pyrophosphate but not in the orthophosphate. Since its intensity overlaps with the silicate intensity in this region, this peak is hard to detect in the total vibrational spectrum. The most reliable marker of P−O−Si links is then probably the high-frequency shoulder in the Si−O stretching band at the top of the spectrum, as described before.

3.4. Electronic Properties. The electronic density of states (EDOS) of the 45S5 glass is plotted in Figure 7, together with two reference EDOS previously obtained for vitreous silica (VS) and soda-lime silicate glass (NCS).[21] The basic electronic properties of wide-gap oxide glasses are determined by their short-range structure,[57] and the similar short-range order also leads to qualitatively similar EDOS for amorphous silica and crystalline quartz.[27,58] The short-range order in 45S5 is not significantly perturbed with respect to higher silica glasses, including VS: therefore, several electronic features of the silicate network of VS and high-silica glasses are retained in the bioactive glass with lower silica content, although the larger structural variety produced by the inclusion of modifier cations and formation of NBOs introduces distortions and additional features in the electronic density of states. An example is the appearance of unoccupied states at the bottom of the conduction band, which reduce the band gap to 3.5 eV, about 1.8 eV narrower than VS and close to the band gap calculated for NCS.[21] The large underestimation of band gaps (compare with the experimental band gap of 9 eV for VS) is typical of computational approaches based on GGA-DFT, which are nonetheless reliable for discussing relative trends and general aspects of the electronic structure of oxide materials[59,60] and glasses:[20,27,28] for instance, the experimental band gap reduction
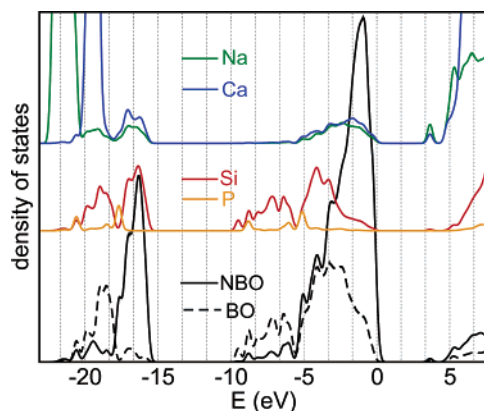
Figure 8. Projection of the EDOS of 45S bioactive glass onto NBO and BO (bottom), Si and P (center), and Na and Ca (top) atoms. The curves are broadened with a Gaussian function of $\sigma = 0.25$ eV width and the highest occupied states are aligned at 0 eV.
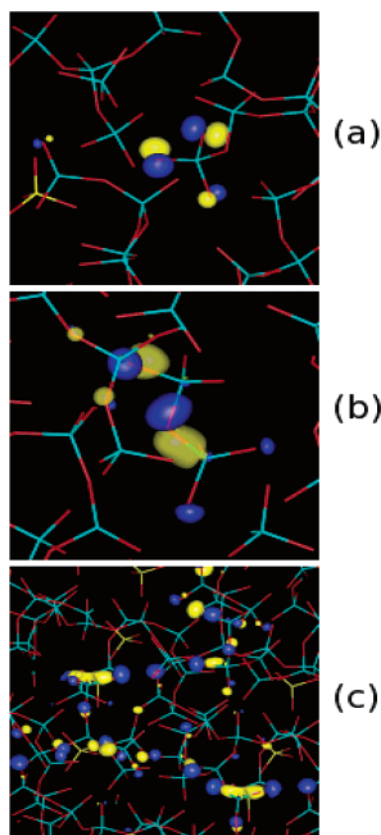

Figure 9. Isosurface plot of Kohn−Sham occupied states representative of (a) NBO nonbonding states at the top of the valence band, (b) Si−BO bonding states, and (c) delocalized BO−NBO states.

of ∼1.5−2 eV in modified glasses compared to VS[57,61,62] is well reproduced in our calculations.

To identify the different contributions, the EDOS was projected onto a set of atomic wavefunctions centered onto each ion, and the resulting projections are shown in Figure 8. The additional states at the bottom of the conduction band are Na 3s and Ca 4s in character, whereas the Si contribution to the conduction band starts to emerge at higher energies, above 5 eV. The Na 3s character of the LUMO already emerged in earlier ab initio cluster calculations on sodium silicate glasses.[63] Figure 8 and direct inspection of the projection coefficients show that the top of the valence band is formed by NBO 2p lone pairs; an isosurface plot of a representative Kohn−Sham state in this region is shown in Figure 9a. Bonding states involving

BO 2p and Si sp³ states, as the one shown in Figure 9b, lie between −5 and −10 eV; phosphorus bonding states also lie at −5 eV. In between these two bands, from −2 to −5 eV, lie delocalized states involving both BO and NBO 2p states mixed with Si 3p: an example is shown in Figure 9c. The higher participation of BOs in bonding states and the nonbonding character of NBO states provide clear evidence of the more covalent character of Si−BO bonds and the higher ionicity of Si−NBO, which entails a higher valence charge density on NBOs, with important effects on the glass structure. For instance, direct effects are the preference of Ca for coordination by NBO, as well as the higher repulsion between two adjacent NBOs mentioned before, which result in a distorted intratetrahedral geometry and influence the geometry of the Na and Ca coordination shell.

A triplet is observed in the EDOS at more negative energies; the lowest energy peak is formed by Na 2p states, whereas the intermediate (−19 eV) and top (−16 eV) peaks result from Ca 3p and Si 2p states overlapping with BO and NBO 2s, respectively. The observed split between BO 2s and NBO 2s, with the NBO states shifted by 2.6 eV at higher energy, is close to previous experiments[64] and DFT calculations[65] on sodium silicates. Inner states (not shown) are found at −38 and −49.5 eV, corresponding to the semicore Ca and Na electrons.

4. Conclusions

This work represents one of the first modeling studies of bioactive glasses using ab initio methods, and, to our knowledge, the first extensive ab initio simulation of these systems performed using relatively large periodic supercells and finite-temperature dynamics to sample a significant number of relevant configurations. Although, as in previous CPMD studies of glasses, only structural properties in the short range are fully relaxed at the ab initio level, the present approach enabled us to reveal with high accuracy the local environment of network-formers silicate and phosphate, as well as of network-modifiers Na and Ca cations. An important role of these cations in connecting and organizing different fragments of the highly disrupted bioglass network has been proposed, which can be a crucial factor when the dissolution of these materials in an aqueous medium (i.e., the first step in their bioactive fixation mechanism) is considered. The decomposition of the vibrational spectrum into the Q^n and atomic contributions allowed us to identify and assign specific vibrational features, which may be useful to support IR and Raman investigations of these materials. Finally, the investigation of electronic properties has allowed the identification of the composition of the valence band and the bottom edge of the conduction band of the bioglass, which are likely to be common to other bioactive compositions as well, and also enabled us to highlight the different electronic distribution of Si−BO and Si−NBO bonds, and discuss significant effects on the local structure.

Supporting Information Available: Radial and angular distribution functions calculated by using only the first half or the second half of the CPMD trajectories. This material is available free of charge via the Internet at http://pubs.acs.org.

References and Notes

(1) *An Introduction to Bioceramics*; Hench, L. L., Wilson, J., Eds.; World Scientific: Singapore, 1993.

(2) Vallet-Regi, M.; Ragel, C. V.; Salinas, A. J. *Eur. J. Inorg. Chem.* **2003**, *6*, 1029.

(3) Hench, L. L. *Science* **1980**, *208*, 826.

(4) Hench, L. L.; Wilson, J. *Science* **1984**, *226*, 630.

(5) Martinez, A.; Izquierdo-Barba, I.; Vallet-Regi, M. *Chem. Mater.* **2000**, *12*, 3080.

(6) Oliveira, J. M.; Correia, R. N.; Fernandes, M. H. *Biomaterials* **2002**, *23*, 371.

(7) Cerruti, M.; Bianchi, C. L.; Bonino, F.; Damin, A.; Perardi, A.; Morterra, C. *J. Phys. Chem. B* **2005**, *109*, 14496.

(8) Serra, J.; Gonzalez, P.; Liste, S.; Serra, C.; Chiussi, S.; Leon, B.; Perez-Amor, M.; Ylanen, H. O.; Hupa, M. *J. Non-Cryst. Solids* **2003**, *332*, 20.

(9) Plotnichencko, V. G.; Sokolov, V. O.; Koltashev, V. V.; Dianov, E. M. *J. Non-Cryst. Solids* **2002**, *306*, 209.

(10) Lin, K. S. K.; Tseng, Y.-H.; Mou, Y.; Hsu, Y.-C.; Yang, C.-M.; Chan, J. C. C. *Chem. Mater.* **2005**, *17*, 4493.

(11) *High Performance Computing in Chemistry*; NIC Series Vol. 25; Grotendorst, J., Ed.; NIC: Jülich, Germany, 2005.

(12) Smith, W.; Greaves, G. N.; Gillan, M. J. *J. Chem. Phys.* **1995**, *103*, 3091.

(13) Horbach, J.; Kob, W.; Binder, K. *J. Phys. Chem. B* **1998**, *103*, 4104.

(14) Tischendorf, B. C.; Alam, T. M.; Cygan, R. T.; Otaigbe, J. U. *J. Non-Cryst. Solids* **2003**, *316*, 261.

(15) Ganster, P.; Benoit, M.; Kob, W.; Delaye, J.-M. *J. Chem. Phys.* **2004**, *120*, 10172.

(16) Linati, G.; Lusvardi, G.; Malavasi, G.; Menabue, L.; Menziani, M. C.; Mustarelli, P.; Segre, U. *J. Phys. Chem. B* **2005**, *109*, 4989.

(17) Du, J.; Corrales, R. L. *Phys. Rev. B* **2005**, *72*, 092201.

(18) Car, R.; Parrinello, M. *Phys. Rev. Lett.* **1985**, *55*, 2471.

(19) Car, R.; de Angelis, F.; Giannozzi, P.; Marzari, N. In *Handbook of Materials Modeling*; Yip, S., Ed.; Springer: Dordrecht, The Netherlands, 2005.

(20) Sarnthein, J.; Pasquarello, A.; Car, R. *Phys. Rev. Lett.* **1995**, *74*, 4682.

(21) Tilocca, A.; de Leeuw, N. H. *J. Mater. Chem.* **2006**, *16*, 1950.

(22) Donadio, D.; Bernasconi, M.; Tassone, F. *Phys. Rev. B* **2004**, *70*, 214205.

(23) Charpentier, T.; Ispas, S.; Profeta, M.; Mauri, F.; Pickard, C. J. *J. Phys. Chem. B* **2004**, *108*, 4147.

(24) Van Ginhoven, R. M.; Jonsson, H.; Corrales, L. R. *Phys. Rev. B* **2005**, *71*, 024208.

(25) Sarnthein, J.; Pasquarello, A.; Car, R. *Science* **1997**, *275*, 1925.

(26) Ispas, S.; Zotov, N.; De Wispelaere, S.; Kob, W. *J. Non-Cryst. Solids* **2005**, *351*, 1144.

(27) Sarnthein, J.; Pasquarello, A.; Car, R. *Phys. Rev. B* **1995**, *12*, 12690.

(28) Ispas, S.; Benoit, M.; Jund, P.; Jullien, R. *Phys. Rev. B* **2001**, *64*, 214206.

(29) *Handbook of Biomaterials Properties*; Black, J., Hastings, G., Eds.; Chapman & Hall:, London, UK, 1998.

(30) Smith, W.; Forester, T. R. *J. Mol. Graph.* **1996**, *14*, 136.

(31) Tilocca, A.; de Leeuw, N. H.; Cormack, A. N. *Phys. Rev. B* **2006**, *73*, 104209.

(32) Tilocca, A.; Cormack, A. N.; de Leeuw, N. H. *Chem. Mater.* **2006**, *submitted.*

(33) Scandolo, S.; Giannozzi, P.; Cavazzoni, C.; de Gironcoli, S.; Pasquarello, A.; Baroni, S. *Z. Kristallogr.* **2005**, *220*, 574.

(34) Perdew, J. P.; Burke, K.; Ernzerhof, M. *Phys. Rev. Lett.* **1996**, *77*, 3865.

(35) Vanderbilt, D. *Phys. Rev. B* **1990**, *41*, 7892.

(36) Tangney, P.; Scandolo, S. *J. Chem. Phys.* **2002**, *16*, 14.

(37) Gaigeot, M.-P.; Sprik, M. *J. Phys. Chem. B* **2003**, *107*, 10344.

(38) Wathelet, V.; Champagne, B.; Mosley, D. H.; Andre, J. M.; Massidda, S. *Chem. Phys. Lett.* **1997**, *275*, 506.

(39) Vollmayr, K.; Kob, W.; Binder, K. *Phys. Rev. B* **1996**, *54*, 15808.

(40) Mead, R.; Mountjoy, G. *J. Phys. Chem. B* **2006**, *110*, 14273.

(41) Lin, C.-C.; Huang, L.-C.; Shen, P. *J. Non-Cryst. Solids* **2005**, *351*, 3195.

(42) Yuan, X.; Cormack, A. N. *J. Non-Cryst. Solids* **2001**, *283*, 69.

(43) The average distances and angles in Figures 1 and 2 can slightly differ from the peak positions of the corresponding radial and angular distribution functions, due to the asymmetry of the latter functions.

(44) Wright, A. C.; Shakhmarkin, B. A.; Vedischeva, N. M. *Glass Phys. Chem.* **2001**, *27*, 97.

(45) Elgayar, I.; Aliev, A. E.; Boccaccini, A. R.; Hill, R. G. *J. Non-Cryst. Solids* **2005**, *351*, 173.

(46) Hoppe, U.; Walter, G.; Kranold, R.; Stachel, D. *J. Non-Cryst. Solids* **2000**, *263−264*, 29.

(47) Brow, R. K. *J. Non-Cryst. Solids* **2000**, *263−264*, 1.

(48) Dubiel, M.; Brunsch, S.; Kolb, U.; Gutwerk, D.; Bertagnolli, H. *J. Non-Cryst. Solids* **1997**, *220*, 30.

(49) McMillan, P. *Am. Miner.* **1984**, *69*, 622.

(50) Brawer, S. *Phys. Rev. B* **1975**, *11*, 3173.

(51) Cerruti, M.; Greenspan, D. C.; Powers, K. *Biomaterials* **2005**, *26*, 1665.

(52) ElBatal, H. A.; Azooza, M. A.; Khalil, E. M. A.; Soltan Monem, A.; Hamdy, Y. M. *Mater. Chem. Phys.* **2003**, *80*, 599.

(53) Gonzalez, P.; Serra, J.; Liste, S.; Chiussi, S.; Leon, B.; Perez-Amor, M. *J. Non-Cryst. Solids* **2003**, *320*, 92.

(54) Arcos, D.; Greenspan, D. C.; Vallet-Regi, M. *Chem. Mater.* **2002**, *14*, 1515.

(55) Li, D.; Fleet, M. E.; Bancroft, G. M.; Kasrai, M.; Pan, Y. *J. Non-Cryst. Solids* **1995**, *188*, 181.

(56) Clayden, N. J.; Pernice, P.; Aronne, A. *J. Non-Cryst. Solids* **2005**, *351*, 195.

(57) Trukhin, A. N. *J. Non-Cryst. Solids* **1995**, *109*, 1.

(58) Koslowski, T.; Kob, W.; Vollmayr, K. *Phys. Rev. B* **1997**, *56*, 9469.

(59) Tilocca, A.; Di Valentin, C.; Selloni, A. *J. Phys. Chem. B* **2005**, *109*, 20963.

(60) Tilocca, A.; Selloni, A. *ChemPhysChem* **2005**, *6*, 1911.

(61) Siegel, G. H., Jr. *J. Phys. Chem. Solids* **1971**, *32*, 2373.

(62) Siegel, G. H., Jr. *J. Non-Cryst. Solids* **1974**, *13*, 363.

(63) Uchino, T.; Iwasaki, M.; Sakka, T.; Ogata, Y. *J. Phys. Chem. B* **1991**, *95*, 5455.

(64) Ching, W. Y.; Murray, L. A.; Lam, D. J.; Veal, B. W. *Phys. Rev. B* **1983**, *28*, 4724.

(65) Liu, F.; Garofalini, S. H.; King-Smith, R. D.; Vanderbilt, D. *Chem. Phys. Lett.* **1993**, *215*, 401.